Experiments in Fluids (2024) 65:41
https://doi.org/10.1007/s00348-024-03782-4

RESEARCH ARTICLE

Simultaneous film temperature and film thickness measurements for jet impingement applications using two-color laser-induced fluorescence

Matthias Koegl[1] · Nikita Mil'to[1] · Lars Zigan[1,2]

Received: 10 October 2023 / Revised: 19 January 2024 / Accepted: 10 February 2024 / Published online: 11 March 2024

Abstract
The study investigates a jet impingement cooling process of a cylindrical geometry relevant for electric and electronic applications. The applied two-color detection technique enables a simultaneous determination of film temperature and film thickness. For this purpose, the heat transfer oil Marlotherm LH was doped with the temperature-sensitive fluorescence tracer nile red. The temperature determination was realized by suitable band pass filters. Preliminary spectral investigations were carried out in terms of varying dye concentration, temperature and film thickness. At high dye concentrations (up to 37.5 mg/L), reabsorption effects lead to a spectral shift toward higher wavelengths with increasing film thickness. Low dye concentrations (0.29 mg/L, 0.59 mg/L) show no film thickness dependent spectral shift. A film temperature investigation at low dye concentration showed no bias of the intensity ratio due to film thickness, i.e., no additional spectral shift toward lower wavelengths was observed. The investigations on the jet impingement setup revealed an increasing film temperature and decreasing film thickness with increasing solid temperature. The average film temperature increases with increasing solid temperature from 298 (solid temperature 298 K) to 308 K (solid temperature 398 K). At higher solid temperatures, the film temperature increases with distance to the stagnation zone. The average film thickness decreases with increasing solid temperature from 0.24 to 0.17 mm. At high solid temperatures, the film temperature increased with radial distance to the stagnation zone. This behavior is caused by the increasing temperature gradient with increasing solid temperature and decreasing viscosity with increasing film temperature.

1 Introduction

The majority of processes of all important sectors (industrial, aerospace, automotive, energy, etc.) are driven or monitored by electric or electronic devices. An optimization of those systems take place in a way that the systems become more and more compact in combination with increased performance. This is only achievable by highly complicated thermal management solutions, which could enable high heat flux dissipation rates in combination with a homogenous temperature distribution. Large heat flux dissipation rates of electric and electronic devices were often realized by immersion cooling (Roe et al. 2022; Pambudi et al. 2022), heat pipes (Pandey and Kumar Gupta 2022; Abdelkareem et al. 2022) and impingement cooling (Celata et al. 2009, 2005; Chen et al. 2002; Jia and Qiu 2003; Klinzing et al. 1992; Labergue et al. 2015). Immersion cooling is mainly used for stationary devices, since it is not the most weight-efficient way of cooling. Here, the cooling liquid surrounds the whole component. This cooling technique is typically used for transformers, generators (stator winding), battery and server applications. In the steel industry, it is utilized for steel treatment. Heat pipes mainly find their application in devices, where high local heat dissipation rates, especially for the minimization of hot spots, are required and often only very limited space is available (e.g., CPUs, Laptops, etc.) (Pandey and Kumar Gupta 2022; Abdelkareem et al. 2022).

Jet or spray impingement cooling is a very efficient cooling method paired with an economic liquid consumption and is described for this reason in more detail (Labergue et al. 2015). Here, an intact jet or small atomized droplets impact

✉ Matthias Koegl
matthias.koegl@unibw.de

[1] Fakultät Für Luft- und Raumfahrttechnik, Institut Für Thermodynamik, Universität der Bundeswehr München (UniBw M), D-85577 Neubiberg, Germany

[2] Erlangen Graduate School in Advanced Optical Technologies (SAOT), Friedrich-Alexander-Universität Erlangen-Nürnberg (FAU), D-91054 Erlangen, Germany

the hot surface. The formed liquid film leads to a high dissipation flux. Here, monodisperse (i.e., uniform size of droplets) (Celata et al. 2009, 2005) and polydisperse sprays (Chen et al. 2002; Jia and Qiu 2003; Klinzing et al. 1992; Al-Ahmadi and Yao 2008) are commonly used. A variety of nozzles were developed over the last decades to create various spray geometries (e.g., full cone, hollow cone, flat fan, air-mist nozzle) (Labergue et al. 2015). The spray impingement process is governed by its individual sub-processes. An optimization of the process requires the improvement of the sub-processes, where a deep understanding is indispensable. Besides the atomization process, the film temperature and the film thickness determine the dissipated heat flux and the required volume flow of the cooling fluid.

Over the last decades, various non-invasive techniques for the characterization of liquid spray structure were developed and improved. Laser-induced fluorescence (LIF) enables a 2D determination of droplet size and temperature (Lemoine and Castanet 2013). LIF/Mie droplet sizing, often referred as d_{32} droplet sizing in the literature, enables a planar determination of absolute droplet size in terms of Sauter mean diameter (SMD, d_{32}) within sprays after adequate calibration (Domann et al. 2002; Frackowiak and Tropea 2010; Koegl et al. 2018a).

The LIF signal is commonly created by a tracer (or "dye") dissolved in a liquid (Mishra et al. 2019) or by the liquid itself (Park et al. 2002). The aromatic components in a multi-component fuel can be excited at UV wavelength, here no additional tracer is needed. The LIF signal, which can be temperature sensitive or insensitive, depends on the absorption and emission properties of the tracer, the solvent itself (e.g., polarity) and the utilized illumination source (e.g., laser, LED, and the respective excitation wavelength and irradiation).

Common tracers for the liquid phase are rhodamine B, fluorescein, pyrromethene, coumarin, Eosin-Y and nile red (Lemoine and Castanet 2013; Mishra et al. 2020; Ulrich et al. 2022; Prenting et al. 2020; Koegl et al. 2022a, 2020a, 2019a, 2022b; Durst et al. 2018). All show a distinctive temperature sensitivity, which could be used for two-color LIF thermometry. This ratio-based technique utilizes the shift and broadening of the fluorescence spectra to determine temperature. Two wisely selected detection channels (commonly realized by suitable band pass filters) enable a temperature determination after calibration.

Since certain solvents show an absorption in the UV region, an excitation in the visible spectrum is recommended. Thus, coumarin, which features a good temperature sensitivity in ethanol (Prenting et al. 2020), may be disadvantageous, since it must be excited in the UV wavelength range. Rhodamine B (Lavieille et al. 2001; Castanet et al. 2009; Labergue et al. 2010; Vetrano et al. 2013; Zhou et al. 2019) is often used in combination with water. Fluorescein (Estrada-Pérez et al. 2011; Chaze et al. 2017; Castanet et al. 2018) and Eosin-Y (Mishra et al. 2019, 2016; Koegl et al. 2019b, 2018b, 2020b) are often applied with water and ethanol. Pyrromethene is commonly utilized in alkanes (dodecane), ketones (3-pentanone) and alcohols (Labergue et al. 2010; Perrin et al. 2015; Palmer et al. 2018, 2016; Wolff et al. 2007; Depredurand et al. 2008; Deprédurand et al. 2011).

Usually, tracers are not soluble in all liquids, there are tracers for polar and tracers for non-polar solvents. For example, Eosin-Y and fluorescein are not soluble in alkanes and gasoline (Durst et al. 2018). Only a few tracers are soluble in alkanes, oils, diesel and gasoline, such as pyrromethene and its derivates (e.g., 597-8C, 597-C8) (Depredurand et al. 2008, 2010). Nile red is mainly used in ethanol/iso-octane mixtures (Koegl et al. 2019a, 2020c, 2021, 2022b).

Until now, a variety of non-invasive techniques for the characterization of liquid film structure have been developed within the last decades. The minimal packing density of high-power applications is determined by the wall heat flux, which is commonly measured by wall-inserted thermocouples (Chen et al. 2002; Al-Ahmadi and Yao 2008; Bernardin et al. 1997). Alternatively, the heat flux can be estimated by infrared thermography (IRT) (Celata et al. 2009, 2005; Gradeck et al. 2012; Dunand et al. 2013). Spray cooling on hot surfaces is commonly classified and quantified by the Weber number and the mass flux (Labergue et al. 2015). The liquid film thickness can be measured by a variety of techniques. Thick films (10–100 µm) are usually determined by laser-induced fluorescence (Fansler and Parrish 2015; Sick and Stojkovic 2001; Cho and Min 2003; Alonso et al. 2010; Yang and Melton 2000) and large films by laser absorption techniques like laser light absorption (up to 5 mm) (Mouza et al. 2000) and laser absorption spectroscopy (up to 1600 µm) (Yang et al. 2018; Pan et al. 2016; Wu et al. 2021). Very thin films (0.1–3 µm) are commonly measured by refractive-index-matched (RIM) imaging, being relevant for fuel film formation and evaporation in IC engines (Maligne and Bruneaux 2011; Drake et al. 2003).

Until now, only a few investigations deal with simultaneous detection of the film thickness and temperature. Schagen et al. studied the film thickness and temperature in a laminar, wavy film of water doped with biacetyl (2,3-butanedione). The developed technique is based on the fact that biacetyl emits fluorescence as well as phosphorescence when illuminated under UV light (Schagen et al. 2006). The local film thickness is determined by the fluorescence, while the film temperature is determined by the phosphorescence. Borgetto et al. investigated the film temperature and thickness of a liquid heptane film along a wall with a low-coherence interferometry technique. The presented technique shows some limitations, such as the minimum possible measurement thickness, which is restricted by the coherence length

of the light source (20 µm @ 1310 nm) and the influence of surface waves on the measurement results (Borgetto et al. 2013). Huang et al. investigated the temperature profile and thickness of a lubricant film during machining based on laser-induced fluorescence. They utilized a combination of a temperature-insensitive probe (fluorescence pink) and temperature-sensitive probe (europium 3 thenoyltrifluoroacetonate (EuTTA) (Huang et al. 2014). Wu et al. investigated the film thickness and temperature of water on a metal plate with diode laser absorption spectroscopy. Their results are in good agreement with thermocouple (temperature deviation: 2.0%) and ultrasonic pulse-echo method (film thickness deviation: 3.3%) measurements (Wu et al. 2021). Collignon et al. investigated thin liquid films flowing down a heated and inclined plane based on a two-color LIF technique. They determined film temperature and film thickness of water simultaneously and quantified the heat transfer coefficient (Collignon et al. 2022).

The present study focuses on film thickness and temperature measurements of a jet impingement cooling process of a cylindrical geometry based on a two-color detection technique developed in an earlier study of the group (Koegl et al. 2022a). For this purpose, nile red dissolved in the heat transfer oil Marlotherm LH, which showed a superior temperature sensitivity in a preliminary investigation, was used (Koegl et al. 2022a). The paper is structured as follows: First, tracer concentration-dependent spectral measurements are carried out for various film thicknesses in a special calibration setup enabling various liquid film thicknesses and temperatures. Here, especially, the influence of the film thickness on the fluorescence spectra due to reabsorption effects are studied. Second, temperature dependent measurements for various film thicknesses at a constant tracer concentration were performed spectrally and by imaging. Third, temperature and liquid film thickness were determined using a jet impingement driven film cooling setup for various solid body temperatures. Finally, a brief conclusion and an outlook is provided.

2 Experimental setup

Two fluorescence setups were designed for the calibration of temperature and liquid film thickness (1) as well as the jet impingement measurements themselves (2). The experimental setups are shown in Figs. 1 and 2. A cw laser (model: LSR532F-2500, 532 nm, 2.5 W, lasever, China) is used to illuminate the probe region in both setups. A remote-controlled external shutter enables a probe illumination only during measurements and possible photo-dissociation effects were kept as low as possible. A beam expander just after the laser exit is used to expand the beam by the factor of 8. A glass plate was applied to monitor the laser fluence simultaneously (model: S425C coupled to PM10D, Thorlabs, USA). The transmitted expanded beam hits the probe region under a 75° angle. This illumination angle allows a perpendicular signal detection of the liquid film. A fiber-coupled spectrometer (model: Maya 2000-Pro, Ocean Optics, USA, wavelength range: 200.5–1120.4 nm, pixels 2048, slit size 25 µm, integration time 100 ms, 20 subsequent spectra were averaged for each measurement) with a detection optic and a camera system (described in the following section) is used for signal detection. The detection optic is placed 100 mm above the probe region and collects the fluorescence signal of an area of 10 mm^2 in the center of the liquid film (see Fig. 1).

2.1 Fluorescence film calibration setup

The calibration of the liquid film thickness was conducted as follows: In order to generate the liquid films with various thickness, heated inserts with various slot depths (0.3–2 mm) were produced. The inserts are made of the same material as the cylindrical surface (aluminum 7075, same charge) described in the subsequent paragraph with the same sandblasted surface treatment to ensure comparability. The coolant-tracer mixture is placed with a syringe in the cavity, a cover glass (thickness 0.16 mm) in combination

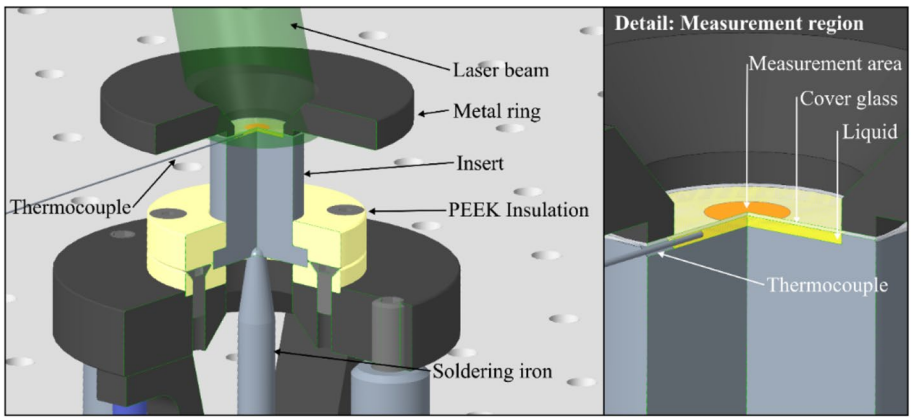

Fig. 1 Optical setup for the spectral measurements

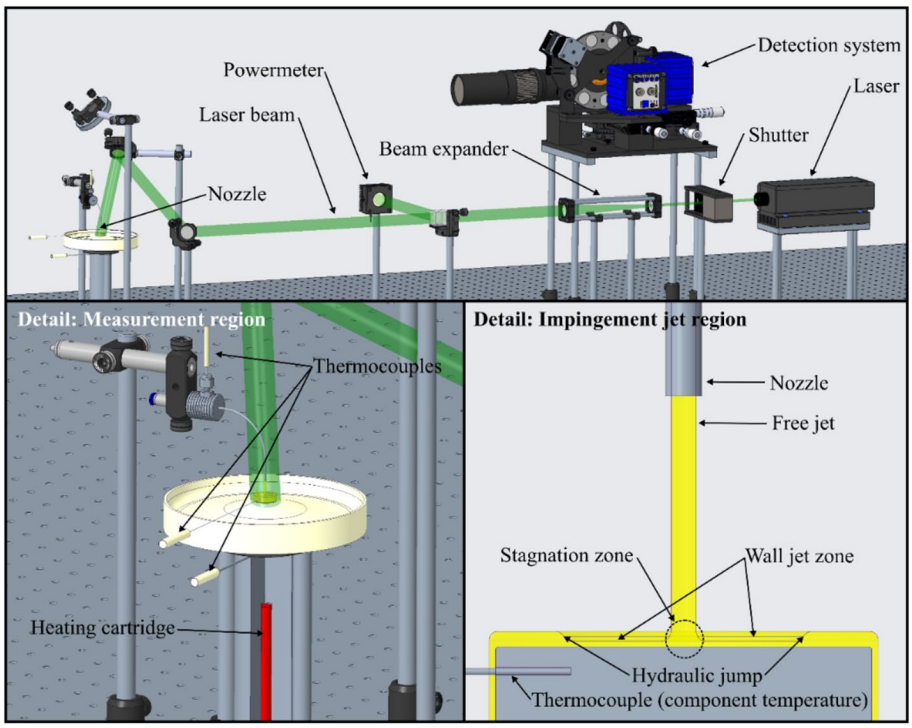

Fig. 2 Optical setup for the fluorescence measurements (top), measurement region (lower left) and impingement jet region (lower right)

with a metal ring ensures accurately adjusted film thickness. A small thermocouple (type K, diameter: 0.25 mm, tc-direct, Kitzingen, Germany; accuracy ±0.3 K) in the liquid volume ensures constant measurement conditions. The temperature of the liquid film is adjusted and kept constant with a modified soldering iron (model WT 1010H, Weller, Besigheim, Germany).

2.2 Jet impingement cooling setup

The optical setup for the impingement jet measurements is shown in Fig. 2. The illumination of the probe region remains the same as already described in the previous section. Instead of the spectrometer, a specially designed camera system, which is equipped with a long-distance microscope (Infinity, Distamax K2, Centennial, CO, USA) is used. The two detection bands of the LIF signals were recorded simultaneously. Here, the signal is divided by a beam splitter right after the objective and the individual signals are recorded with two identical sCMOS cameras (LaVision GmbH, Goettingen, Germany; 2560 × 2160 pixels, nominal pixel resolution 8.39 µm/pixel). A geometric calibration (mapping) is performed in Matlab® to ensure proper alignment of the two detection channels. The LIF signal bands are detected by using appropriate filters (Edmund optics: filter1: 568 nm (#65–221), filter2: 632 nm (#65–166); 10 FWHM), which were selected in a previous study (Koegl et al. 2022a). The coolant-tracer mixture is pumped in a closed loop (2000ml liquid volume) with an adjustable modified gear pump (model: UP3, Marco s.p.a., Castenedolo, Italy). The fluid went via an adjustable bypass through a seamlessly drawn stainless steel tube (1 mm inner diameter, nozzle velocity: 2.03 m/s) and hits the heated cylindrical surface (diameter 15 mm) perpendicular in the center. The surface (aluminum 7075) is heated with a heating cartridge (model: RS PRO 200W, RS-Components, Frankfurt am Main Germany) driven by a laboratory controller (model: LR 316, Jumo, Fulda, Germany). The Reynolds and Prandtl numbers at 293 K are calculated at the nozzle outlet to be Re = 508 and Pr = 48.7, respectively. Fluid properties are also provided in Table 1.

The solid temperature T_S of the cylinder is measured 1 mm below the surface with a thermocouple (type K, tc-direct GmbH, Kitzingen, Germany; accuracy ±0.3 K). The surface is sandblasted to achieve a homogeneous surface without any manufacturing traces and ensure a homogeneous reflection behavior. The temperature of the coolant circuit is kept constant by a counterflow heat exchanger driven by

Table 1 Physical properties of Marlotherm LH (Eastman chemical company, Marlotherm 2022; McClintock and Meyers 2003)

Property	Unit	Marlotherm LH
Density	g/cm^3	9.960 (293 K)
Heat conductivity	W/(m·K)	0.132 (293 K)
Kinematic viscosity	mm^2/s	4.00 (293 K)
Specific heat	kJ/(kg·K)	1.614 (293 K)

a recirculating thermostat (model: CP50, Thermo Fisher Scientific, Waltham, MA, USA). Multiple thermocouples (type K, tc-direct GmbH, Kitzingen, Germany) at the nozzle outlet, before the pump and after the cooler ensure constant measurement conditions.

2.3 Coolant and tracer used

In the present study, the emission signal of the heat transfer fluid Marlotherm LH (Sasol Germany GmbH, Hamburg, Germany) in combination with the fluorescence tracer nile red was investigated. The chemical and physical properties of Marlotherm LH are shown in Table 1.

The fluorophore nile red ($C_{20}H_{18}N_2O_2$, Sigma Aldrich: Bellefonte, PA, USA) was initially used in the field of microfluidic systems and biology (Zhang et al. 2018; Lin et al. 2014; Greenspan and Fowler 1985). Recent studies applied the tracer for planar droplet sizing of fuel sprays, two-color thermometry and composition measurements (Koegl et al. 2019a, 2020c, 2021, 2022a). The aromatic ring structure features polar substituents. A high sensitivity toward the chemical and physical environment of surrounding solvent molecules is attributed by the polar substituents (Kalathimekkad et al. 2015). Nile red is soluble in alkanes and real-world fuels (multi-component fuels) (Durst et al. 2018). A minimum of 3.75 mg of nile red was weighted with a high-precision analytical scale (Mettler Toledo XS 205, proofed repeatability 0.05 mg). The tracer was completely dissolved in the investigated heat transfer oil. Nile red has a melting point of 476–479 K (Nile red 2022), but this temperature is above the maximum tested temperature in the present setup. For the present study, tracer concentrations of 0.29–37.5 mg/L were investigated. The various investigated tracer concentrations were generated by diluting the initial oil–tracer mixtures.

2.4 Two-color detection scheme for temperature determination

The temperature of the liquid-dye mixture can be determined with the intensity ratio r of the two detection channels CH1 and CH2, respectively. After the determination of the local temperature, the film thickness can be determined by the intensity ratio r and the intensity of either CH1 or CH2. In a preliminary spectral study, we determined the intensity ratios for the dye in different oils for a dye concentration of 9.38 mg/L. The fit parameters and the corresponding coefficient of determination can be found in Koegl et al. 2022a. However, in the present study, the dye concentration is much lower (0.59 mg/L) resulting in a significantly reduced fluorescence reabsorption. Additionally, a different detection system is applied as in the previous work, so that the fit parameters have to be calculated again. The ratio r can be determined using the ratio of the two products of the transmission curves τ of the respective filters and the spectral fluorescence emissions I_{Ch1} and I_{CH2} (when other efficiencies of the optical setup (e.g., cameras) are neglected):

$$r = \frac{\sum \tau_{\text{Filter\_568 nm}} \cdot I_{\text{LIF}}}{\sum \tau_{\text{Filter\_632 nm}} \cdot I_{\text{LIF}}} = \frac{I_{\text{CH1}}}{I_{\text{CH2}}} \quad (1)$$

3 Results

This section is structured as follows. First, tracer concentration-dependent spectral measurements were carried out for various film thicknesses at constant temperature. Here, the influence of the film thickness on the spectra due to reabsorption effects was studied. Second, temperature and film thickness were calibrated spectrally and by imaging at a constant optimal tracer concentration. Afterward, a jet impingement cooling process is investigated, and the film temperature and film thickness are determined at various liquid volume flows. All spectral results are presented in the visible wavelength range (380–780 nm), which is most relevant for the absorption and emission of nile red (Koegl et al. 2019a).

3.1 Spectral measurements

3.1.1 Film thickness variation

The emission spectra of nile red at various concentrations dissolved in Marlotherm LH for various film thicknesses are shown in Fig. 3.

Here, the peak regions are magnified, since an occurring spectral shift is important for the measurement uncertainty of the applied technique. The measurements revealed a spectral shift of the maxima and both flanks toward larger wavelengths with increasing film thickness. This behavior is caused by reabsorption effects, since the fluorescence at lower wavelengths is in the absorption band and may lead to an excitation of the tracer. An investigation on the absorption (and fluorescence) of the used tracer-oil mixture was already performed in a previous paper of the group (Koegl et al. 2022a). A decrease of the tracer concentration leads to a decrease of the film thickness dependent spectral shift, since the reabsorption effect is reduced with lower tracer concentration. A two-color ratio technique for the determination of the temperature is only applicable, when the temperature dependent spectral shift is not affected by a variation in film thickness.

On the other hand, a sufficient signal to noise ratio (and thus large tracer concentrations in principle) is indispensable for reliable measurements. To achieve a good signal to

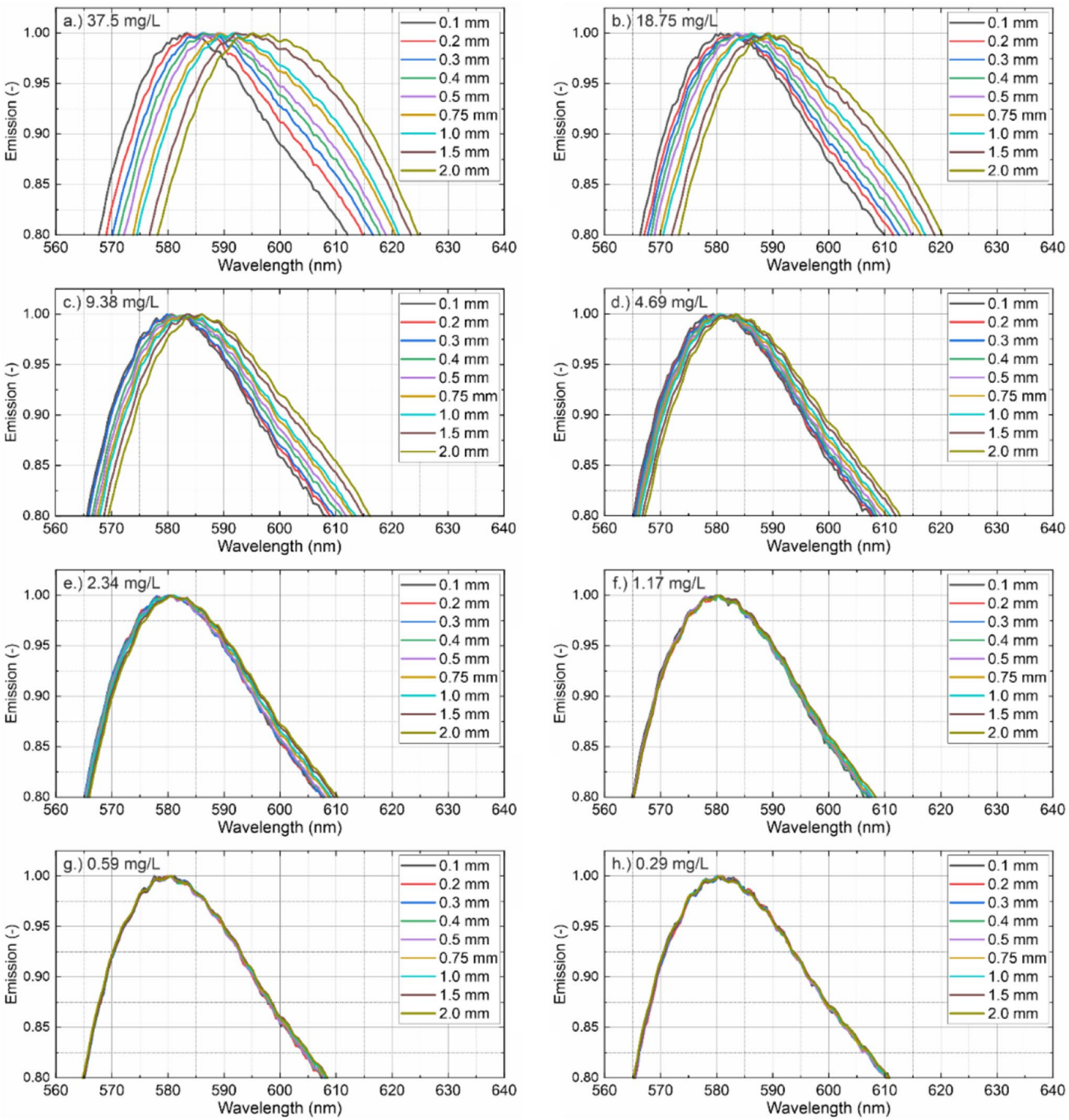

Fig. 3 Normalized emission spectra of nile red at various concentrations and film thicknesses, 298 K

noise ratio, a high laser fluence would be beneficial. However, this could be problematic as tracer dissociation may occur. Thus, cw lasers (continuous wave) and LEDs are advantageous compared to pumped laser systems. These illumination systems enable a longer exposure time (here 100 ms), while pumped lasers illuminate usually between 6 and 8 ns. CW lasers feature a very narrow spectral emission (down to 1 nm FWHM for Raman lasers) compared to LEDs (30 nm FWHM and higher). Previous investigations with the same tracer–oil mixture in a larger volume revealed no photo-dissociation effects within 20 min at constant laser illumination with an pulsed Nd:YAG laser (Koegl et al. 2022a). The cw laser in the current setup in combination with the high radiant power, long illumination duration and low film thicknesses of the spectral setup (see Fig. 1) leads to significant photo-dissociation effects, which have to be

Table 2 Film thickness dependent spectral shift of the emission peak for various dye concentrations

Concentration (mg/L)	Spectral shift (nm)
37.5	13.6
19.75	8.2
9.38	5.5
4.69	3.9
2.34	1.4
1.17	0.4
0.59	0.1
0.29	0.1

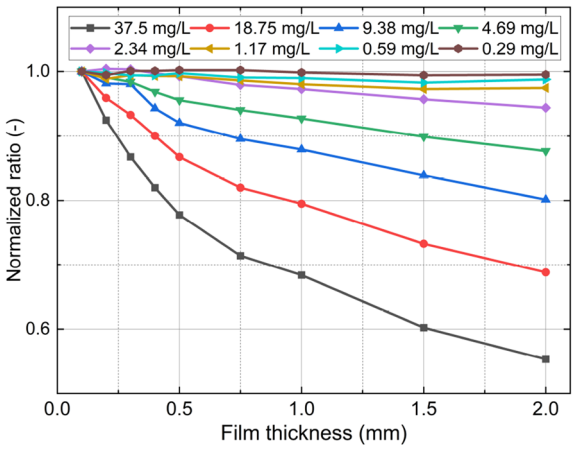

Fig. 4 Concentration-dependent signal ratio (normalized to the emission at 0.1 mm for all concentrations, 298 K

taken into account (i.e., by changing the tracer–liquid mixture after each measurement). The photo-dissociation effect for the impingement cooling setup is neglectable, since the volume (2000 mL) for the operating time is high enough. The spectral shift within the investigated thickness interval (0.1–2.0 mm) for various dye concentrations is shown in Table 2. The spectral shift of 13.6 nm (@ 37.5 mg/L) decreased to 0.1 nm (@ 0.59 mg/L and 0.29 mg/L) with decreasing tracer concentration. Since the spectral shifts of 0.59 mg/L and 0.29 mg/L are similar and to achieve a good signal to noise ratio with the current setup, 0.59 mg/L is applied for the following investigations.

The corresponding signal ratio (filter 568 nm/filter 632 nm) for various concentrations and film thicknesses is shown in Fig. 4.

The ratio is normalized to the emission at 0.1 mm for better visualization. The ratio is calculated according to Eq. (2). The transmission curves of the two band pass filters are estimated with two rectangular filters used for the intensity ratio of the subsequent imaging experiments (568 nm: 563–573 nm; 632 nm: 627–637 nm). The ratio for the tracer concentration of 37.5 mg/L changes by −44.7% from 0.1 to 2.0 mm. Tracer concentrations of 0.59 mg/L and 0.29 mg/L show a change of 1.71% and 0.79%, respectively. The two-color technique for temperature is only applicable, if the signal ratio does not change with film thickness. The results show that only low dye concentrations (0.59 mg/L and 0.29 mg/L) lead to a constant signal ratio for various film thicknesses.

3.1.2 Temperature study

The temperature dependent film thickness is measured spectrally and by imaging. The planar measurements were conducted with a detection system (see imaging setup) with respective band pass filters. For the 2D measurements, the fluorescence intensities within a region of interest (ROI, see Fig. 1) are summed up and the ratio is determined. The emission spectra of nile red dissolved in Marlotherm LH for various temperatures and film thicknesses are shown in Fig. 5. Here, the peaks are magnified again, since the spectral shift is important for the measurement uncertainty of the applied technique. The measurements revealed a spectral shift of 6.3 nm of the maxima and both flanks toward lower wavelengths with temperature. The spectra are not affected by the film thickness, since the dye concentration is low enough (see previous section).

The temperature-dependent signal ratios of nile red (0.59 mg/l) dissolved in Marlotherm LH for various film thicknesses are shown in Fig. 6. An increase in temperature leads to an increase of the signal ratio. The ratios for various film thicknesses are close together. The deviation of the intensity ratio decreases slightly with increasing temperature (303 K: ±4.1%; 338 K: 1.9%). The average measurement uncertainty of the intensity ratio for the investigated film thickness interval for the spectral measurements is ±2.8%.

3.2 Imaging measurements

The previous spectral measurements determined the dye concentration and the temperature dependent behavior of the emission signal. These measurements revealed that only low dye concentrations are sufficient for an accurate determination of temperature and film thickness. For the following measurements, a dye concentration of 0.59 mg/L was used. The camera-based detection system has a different efficiency (filters, lenses, mirrors and quantum efficiency of the sCMOS, etc.) in comparison to the spectroscopic setup. The temperature and film thickness dependent measurements at a fixed dye concentration have to be repeated, to ensure an adequate calibration of the setup. For the temperature and thickness dependent calibration measurements (see experimental setup Fig. 1), the average intensities of a square area (301 pixel× 301 pixel) were used for the evaluations. The two detection channels

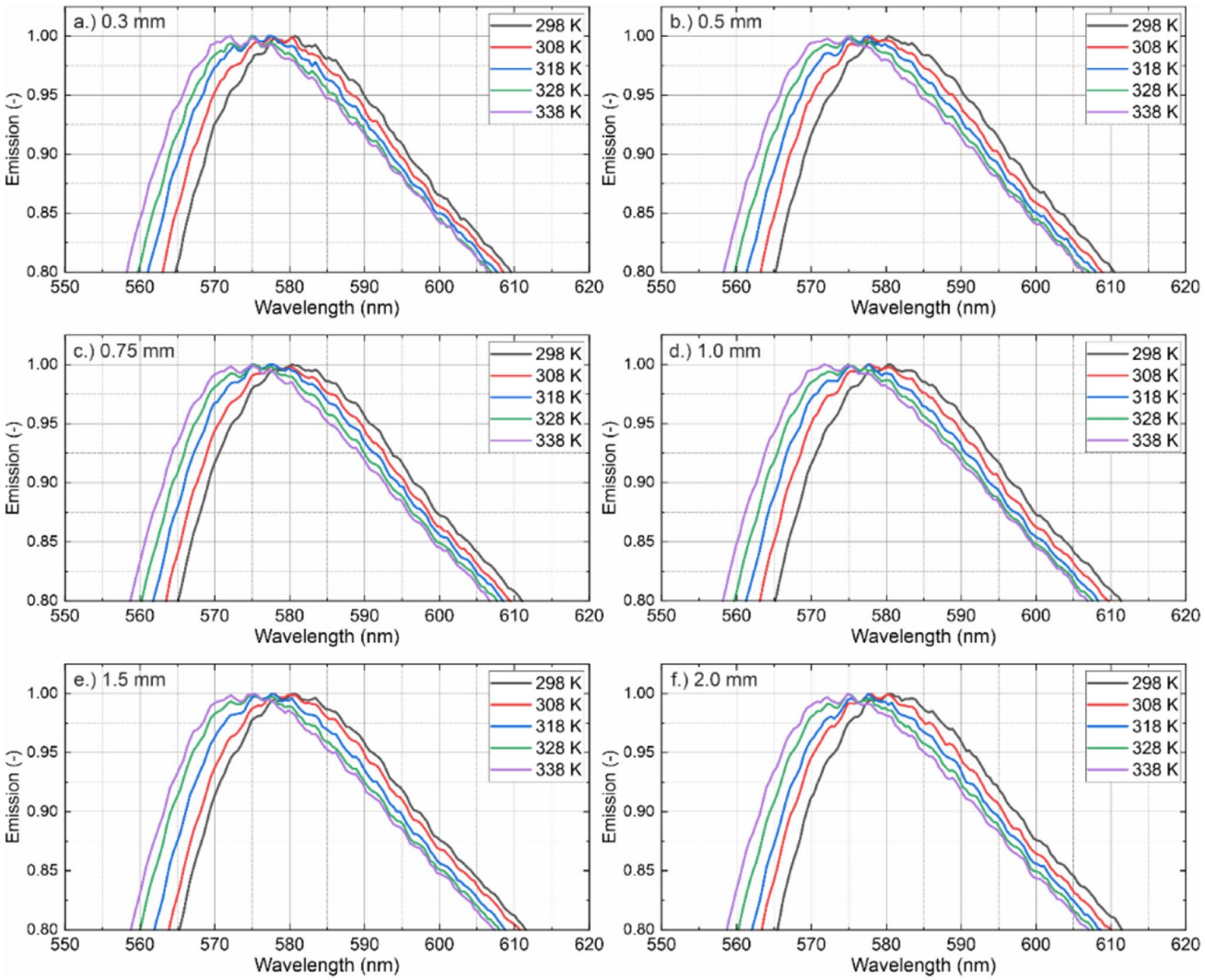

Fig. 5 Normalized emission spectra of nile red at various temperatures and film thicknesses, 0.59 mg/L

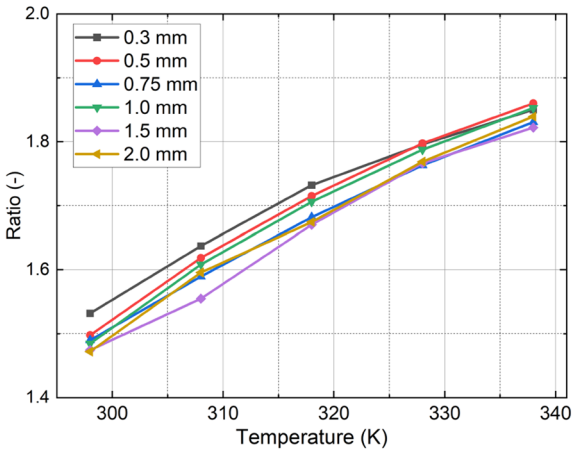

Fig. 6 Temperature calibration of the signal ratio and film thickness dependency in spectral calibration measurements. The liquid temperature was measured in the cavity using a thermocouple

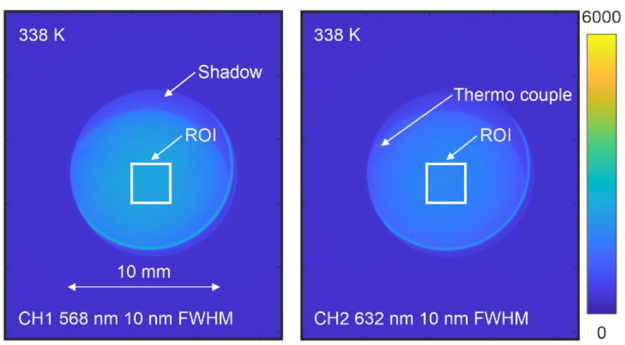

Fig. 7 Raw images showing the signal intensity of the detection channels CH1 and CH2 for the film thickness calibration measurements, film thickness 0.3 mm and film temperature 338 K

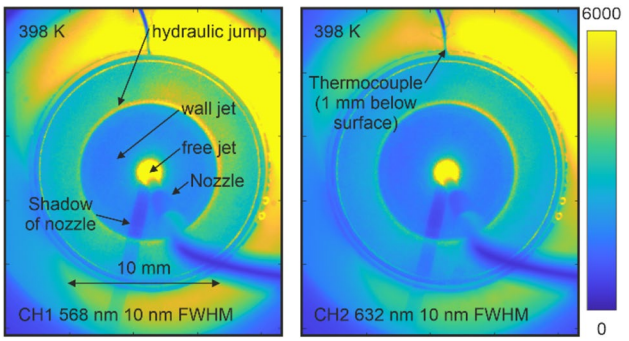

Fig. 8 Signal intensity of the detection channels CH1 and CH2 in the jet impingement measurements, solid temperature 398 K

and the corresponding ROI of a film thickness of 0.3 mm at a temperature of 338 K are shown in Fig. 7. The signal intensities and corresponding coefficients of variation (defined as standard deviation divided by the mean value) in the respective ROI of both detection channels CH1 and CH2 (CH1: 0.045; CH2: 0.047) are similar, therefore CH1 was used for the determination of the film thickness. Standard deviations of various temperatures will be discussed subsequently. The tilted illumination leads to a shadow region, caused by the metal ring, which is visible in the upper part of the images.

The imaging of the impinging jet (see experimental setup Fig. 2) is shown in Fig. 8. Here, the two detection channels are shown for a solid temperature of the heating components (measured 1 mm below the surface) of 398 K. The tilted illumination again leads to a shadow region, caused by the tube/nozzle, which is visible in the lower part of the images. The jet impingement process is shown in Fig. 2 and can be separated in different zones. The stagnation zone is defined as the area, where the free jet impinges the flat surface. Afterward, a wall-jet zone is generated, which ends at the location, where the hydraulic jump is generated. The hydraulic jump is formed by a large increase of the film thickness and a significantly decrease of the film velocity. The impingement heat transfer takes mainly place in the stagnation zone and the wall-jet zone (Liu et al. 2014). For the experiments, only the wall-jet zone can be evaluated, since so-called morphologic-dependent resonances, MDRs (or whispering gallery modes) at larger wavelengths may cause significant measurement uncertainties (Koegl et al. 2022b). A two-dye approach could suppress the MDRs, which could be part of future work. The second dye, with an absorption band located at the wavelengths where MDRs usually occur, would lead to a suppression of the lasing signal (Palmer et al. 2016; Ulrich et al. 2023). However, the temperature of the wall-jet region is the scope of the present paper, since it governs the heat transfer and no MDRs were observed there. The temperature and film thickness are determined by the calibration curves derived from the fluorescence film calibration setup (see Fig. 1).

The temperature and film thickness dependent intensity ratio and the respective spatial standard deviations in the ROI are shown in Fig. 9. Since the intensity ratio is not dependent on the film thickness for low tracer concentrations (see Fig. 4), an average for the determination of the fit equation was applied. The temperature T_{Film} can be determined by the intensity ratio r with the following polynomial equation:

$$T_{\mathrm{Film}} = 361.36066 - 207.4571r + 140.39784r^2 \quad (2)$$

This polynomial fit of the regression function gave the best value of the coefficient of determination R^2, which is 0.99851. The coefficient of determination is a statistical measure of how well a regression curve approximates the experimental data. The spatial standard deviations of the intensity ratio are between 0.0365 and 0.0795, which corresponds to a COV between 3.4 and 5.9%. The temperature sensitivity decreases almost linearly from 1.02 at 298 K to 0.51 at 338 K.

The film thickness t_{Film} is dependent on the signal intensity I_{CH1} and the temperature T_{Film} (see Fig. 5). Since the measurements revealed a film thickness and film temperature of the operating points (impinging jet) in the interval of [298–318 K] and [0.2–0.5 mm], a fit of the mean values for the signal intensity of CH1 is sufficient. The measurement points, the corresponding fit and standard deviations are shown in Fig. 10. The nonlinear increase of film thickness with signal intensity is caused by extinction effects, which reduce the average illumination fluence in

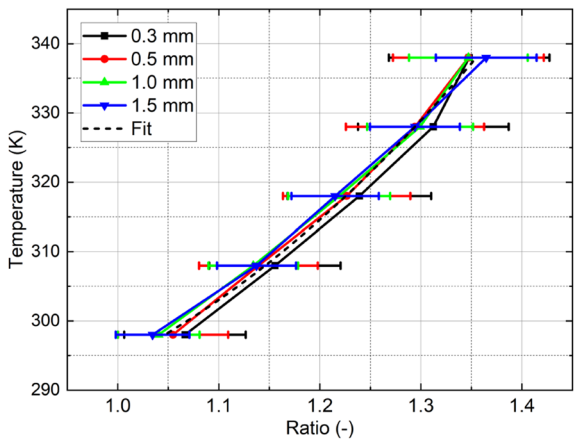

Fig. 9 Calibration of film temperature- and film thickness-dependent intensity ratio determined by using the imaging setup. Error bars refer to the spatial precision (standard deviation) in the ROI

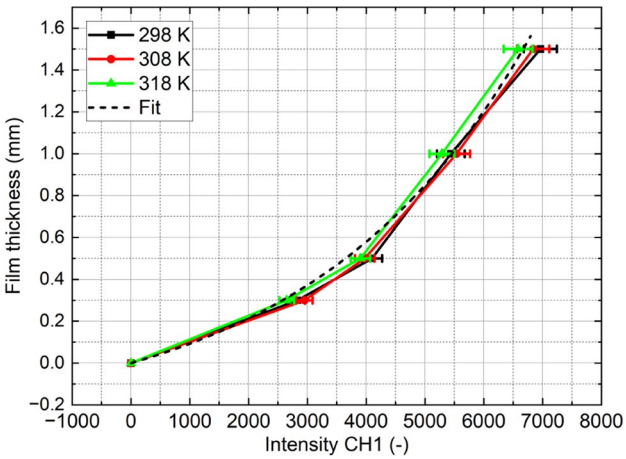

Fig. 10 Fit for film thickness as a function of the temperature and the signal intensity I_{CH1}. Error bars refer to the spatial precision (standard deviation) in the ROI

the liquid film and signal reabsorption. The film thickness t can be described by the following exponential fit equation ($R^2 = 0.99377$):

$$t_{\text{Film}} = 0.10248\,\frac{I_{\text{CH1}}}{3452.48101} + 0.10248\,\frac{I_{\text{CH1}}}{3836.09001} + 0.10248\,\frac{I_{\text{CH1}}}{4219.69901} - 0.30745 \quad (3)$$

It should be noted that the calibration process is conducted by using a cover glass, while the actual film measurements are conducted in an uncovered film. This introduces differences in signal intensities between calibration and film measurements. The thickness of the cover glass used is 0.16 mm. The transmission at 532 nm is in the range of 0.92. However, reflexion effects of the uncovered film surface will also reduce the laser fluence. This has only an impact on the film thickness determination and can be corrected in the wall film measurements by adopting the laser fluence. Fluorescence scattering effects in the calibration cell may occur as well, but this is more distinct in the side wall region (visible in form of the bright rings, but this is outside the ROI of the calibration). The temperature determination is a ratio-based method, which is less affected by variations in laser fluence.

The spatial variation (COV) of 3.4–4.7% is mainly introduced by inhomogeneities in laser illumination. For complex curved geometries (such as wavy liquid films), a uniform illumination is usually not possible. Non-uniform illumination will only cause measurement uncertainties for the determination of the film thickness (and not for the thermometry), since it is based on the intensity of one detection channel only.

The intensities of the two detection channels, the corresponding intensity ratio, the temperature and the film thickness fields at various solid temperatures are shown in Fig. 11. The corresponding solid and initial jet temperatures are shown in Table 3. Additional horizontal-line plots of the temperature and film thickness distribution are shown in Figs. 12 and 13.

The signal intensities of both detection channels are in the same range at low temperature. The intensity ratio increases with solid temperature, since the emission spectra were shifted toward lower wavelengths (see Fig. 5) and consequently, CH1 increases compared to CH2. Since the wall-jet zone is not completely symmetric (orientation of the jet nozzle and disturbed flow field caused by elbow in the nozzle pipe), the film thickness on the left side is smaller in comparison to the right side (see also Fig. 13). This leads to slightly higher film temperatures on the left in comparison to the right side (see Fig. 12). The spatially averaged film temperature increases with increasing solid temperature from 298 to 308 K. The temperature difference between the left and the right side for elevated temperatures ($\geq$ 348 K) is approximately 4 K.

The solid temperature was measured on the top of the cylinder (see Fig. 8), thus the heat transfer process leads to a varying temperature field over the cylindrical surface. At higher solid temperatures, the film temperature increases with distance to the stagnation zone. This behavior is caused by the increasing temperature gradient with increasing solid temperature and decreasing viscosity with increasing film temperature. The average film thickness decreases with increasing solid temperature from 0.3 to 0.2 mm (see Fig. 13). This behavior is again caused by the reduced viscosity at higher temperatures and obviously larger flow velocity generated at the heated wall.

It should be noted that the thermal boundary layer at the bottom of the film might influence the measurement results. Only spatially averaged temperatures can be provided and no information with the film thickness is available. If the film thickness is smaller than the theoretical thermal boundary layer, this will affect the temperature measurements. This effect could be included also in the resulting fit curve for the intensity ratio of the calibration, which is averaged for different film thicknesses.

4 Conclusions and future work

Film thickness and film temperature of a jet impingement cooling process of a simplified heated cylindrical geometry were investigated based on a two-color LIF technique. The LIF signal was created by admixture of the fluorescent dye nile red to Marlotherm LH. A spectral investigation revealed a dye concentration dependence of the emission spectra for various film thicknesses. At high dye concentrations (up to 37.5 mg/L) reabsorption effects lead to a spectral shift toward higher wavelengths with increasing film thickness. Low dye concentrations (0.29 mg/L, 0.59 mg/L) show no

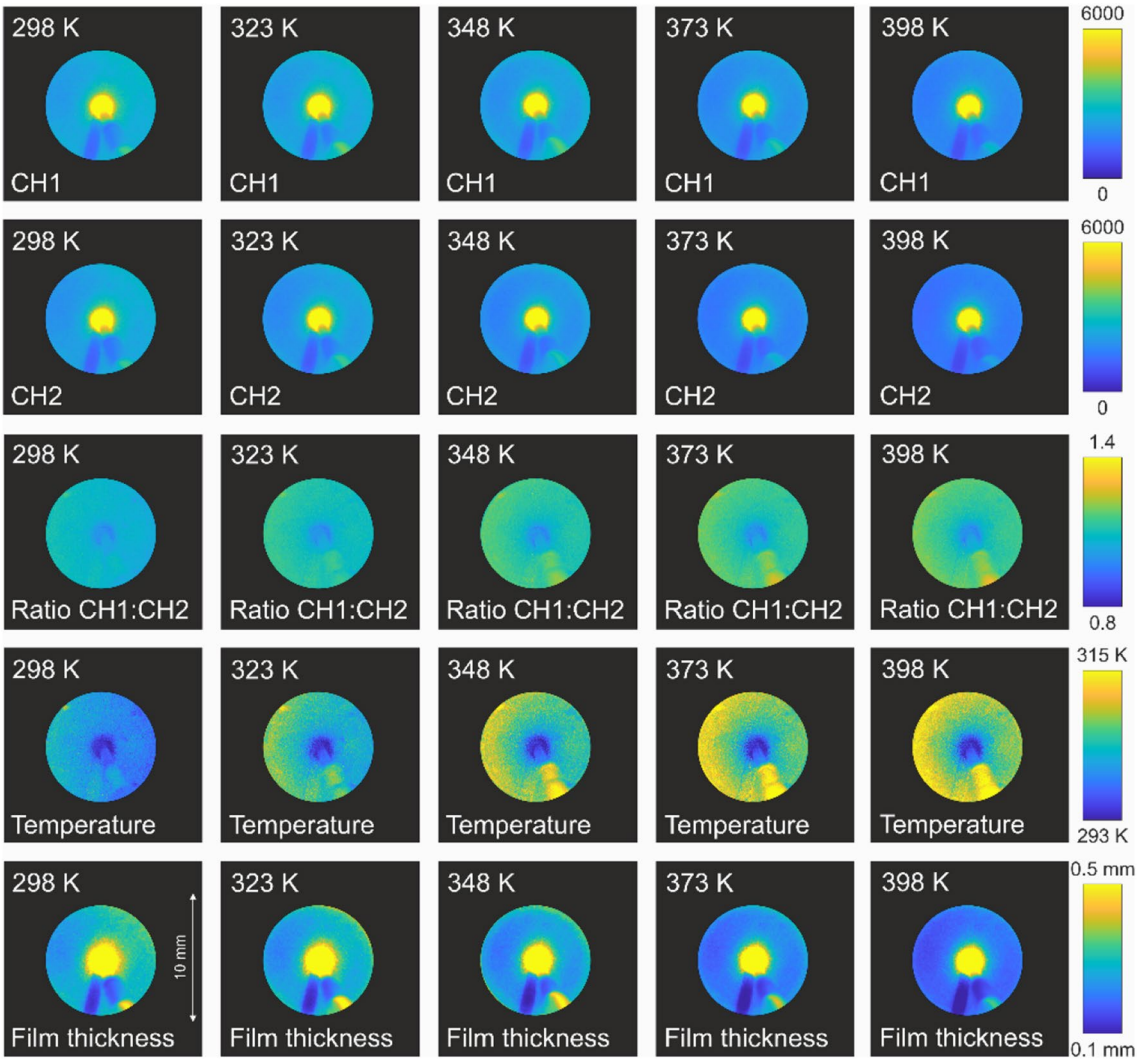

Fig. 11 Signal intensities (top, first two lines), signal ratio (center line), temperature and film thickness fields for various solid temperatures

Table 3 Solid and initial jet temperatures (solid temperatures ±0.3 K) measured by thermocouples

Solid temperature (K)	298	323	348	373	398
Jet temperature (K)	295.4	295.9	295.6	295.9	295.9

film thickness dependent spectral shift. A film temperature investigation at low dye concentration showed no bias of the intensity ratio due to film thickness, i.e., no additional spectral shift toward lower wavelengths was observed.

The investigations on the jet impingement setup revealed an increasing film temperature and decreasing film thickness with increasing solid temperature. The average film temperature increases with increasing solid temperature from 298 (solid temperature 298 K) to 308 K (solid temperature 398 K). At higher solid temperatures,

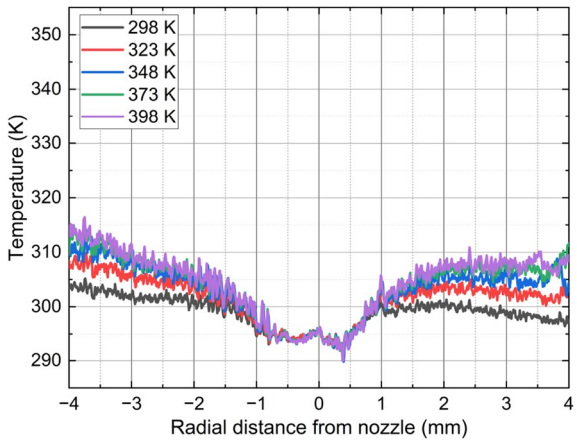

Fig. 12 Horizontal temperature distribution of the liquid film for various solid temperatures

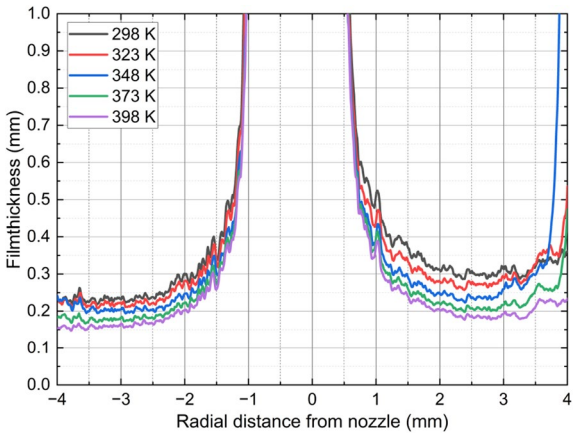

Fig. 13 Horizontal film thickness distribution of the liquid film for various solid temperatures

the film temperature increases with distance to the stagnation zone. The average film thickness decreases with increasing solid temperature from 0.24 to 0.17 mm. At high solid temperatures, the film temperature increased with radial distance to the stagnation zone. This behavior is caused by the increasing temperature gradient with increasing solid temperature and decreasing viscosity with increasing film temperature.

The temperature sensitivity of the intensity ratio was 0.51–1.02%/K, the spatial temperature precision was 3.4–5.9% and the spatial thickness precision 3.4–4.7%. The presented technique works well on the simplified cylindrical geometry. The application of planar diagnostics for jet and spray measurements on real geometries (heat sinks and other complex geometries) is part of future work. The experimental setup could be extended with LIF/Mie droplet sizing in spray configurations, to measure besides the temperature and thickness of the cooling films the droplet size distribution of sprays simultaneously.

Author contributions MK conceptualized the experiment. MK designed the optical setup. NM and MK performed the measurements. MK performed the data evaluation. MK supervised the experiments. MK wrote the paper. LZ performed funding acquisition and reviewed and edited the paper. All authors have read and agreed to the published version of the manuscript.

Funding Open Access funding enabled and organized by Projekt DEAL. We acknowledge financial support by Universität der Bundeswehr München (UniBw M). Open Access funding enabled and organized by Project DEAL.

Data availability Data can be shared upon request.

Declarations

Conflict of interest The authors declare no competing interests.

Ethical approval Not applicable.

References

Abdelkareem MA, Maghrabie HM, Abo-Khalil AG, Adhari OHK, Sayed ET, Radwan A, Rezk H, Jouhara H, Olabi AG (2022) Thermal management systems based on heat pipes for batteries in EVs/HEVs. J Energy Storage 51:104384. https://doi.org/10.1016/j.est.2022.104384

Al-Ahmadi HM, Yao SC (2008) Spray cooling of high temperature metals using high mass flux industrial nozzles. Exp Heat Transf 21(1):38–54. https://doi.org/10.1080/08916150701647827

Alonso M, Kay PJ, Bowen PJ, Gilchrist R, Sapsford S (2010) A laser induced fluorescence technique for quantifying transient liquid fuel films utilising total internal reflection. Exp Fluids 48(1):133–142. https://doi.org/10.1007/s00348-009-0720-8

Bernardin JD, Stebbins CJ, Mudawar I (1997) Mapping of impact and heat transfer regimes of water drops impinging on a polished surface. Int J Heat Mass Transf 40(2):247–267. https://doi.org/10.1016/0017-9310(96)00119-6

Borgetto N, André F, Galizzi C, Escudié D (2013) Simultaneous film thickness measurement and wall temperature assessment by Low-Coherence Interferometry. Exp Thermal Fluid Sci 44:512–519. https://doi.org/10.1016/j.expthermflusci.2012.08.013

Castanet G, Liénart T, Lemoine F (2009) Dynamics and temperature of droplets impacting onto a heated wall. Int J Heat Mass Transf 52(3):670–679. https://doi.org/10.1016/j.ijheatmasstransfer.2008.07.024

Castanet G, Chaze W, Caballina O, Collignon R, Lemoine F (2018) Transient evolution of the heat transfer and the vapor film thickness at the drop impact in the regime of film boiling. Phys Fluids 30:122109. https://doi.org/10.1063/1.5059388

Celata GP, Cumo M, Lombardo C, Mariani A, Saraceno L (2005) Experimental result on rewetting of hot surfaces by droplet impingement. Exp Thermal Fluid Sci 29(3):275–285. https://doi.org/10.1016/j.expthermflusci.2004.05.007

Celata GP, Cumo M, Mariani A, Saraceno L (2009) A comparison between spray cooling and film flow cooling during the rewetting of a hot surface. Heat Mass Transf 45:1029–1035. https://doi.org/10.1007/s00231-007-0265-4

Chaze W, Caballina O, Castanet G, Lemoine F (2017) Spatially and temporally resolved measurements of the temperature inside droplets impinging on a hot solid surface. Exp Fluids 58(8):96. https://doi.org/10.1007/s00348-017-2375-1

Chen R-H, Chow LC, Navedo JE (2002) Effects of spray characteristics on critical heat flux in subcooled water spray cooling. Int J Heat Mass Transf 45(19):4033–4043. https://doi.org/10.1016/S0017-9310(02)00113-8

Cho H, Min K (2003) Measurement of liquid fuel film distribution on the cylinder liner of a spark ignition engine using the

laser-induced fluorescence technique. Meas Sci Technol 14:975. https://doi.org/10.1088/0957-0233/14/7/310
Collignon R, Caballina O, Lemoine F, Markides C, Castanet G (2022) Heat transfer enhancement in wavy films falling on a heated inclined plate. SSRN Electron J. https://doi.org/10.2139/ssrn.4172033
Depredurand V, Miron P, Labergue A, Wolff M, Castanet G, Lemoine F (2008) A temperature-sensitive tracer suitable for two-colour laser-induced fluorescence thermometry applied to evaporating fuel droplets. Meas Sci Technol. https://doi.org/10.1088/0957-0233/19/10/105403
Depredurand V, Castanet G, Lemoine F (2010) Heat and mass transfer in evaporating droplets in interaction: Influence of the fuel. Int J Heat Mass Transf 53(17–18):3495–3502. https://doi.org/10.1016/j.ijheatmasstransfer.2010.04.010
Deprédurand V, Delconte A, Lemoine F (2011) Combined PDA and LIF applied to size–temperature correlations measurements in a heated spray. Exp Fluids 50(3):561–571. https://doi.org/10.1007/s00348-010-0956-3
Domann R, Hardalupas Y, Jones AR (2002) A study of the influence of absorption on the spatial distribution of fluorescence intensity within large droplets using Mie theory, geometrical optics and imaging experiments. Meas Sci Technol 13:280–291. https://doi.org/10.1088/0957-0233/13/3/308
Drake MC, Fansler TD, Solomon AS, Szekely GA (2003) Piston fuel films as a source of smoke and hydrocarbon emissions from a wall-controlled spark-ignited direct-injection engine. SAE Technical Paper, https://doi.org/10.4271/2003-01-0547
Dunand P, Castanet G, Gradeck M, Maillet D, Lemoine F (2013) Energy balance of droplets impinging onto a wall heated above the Leidenfrost temperature. Int J Heat Fluid Flow 44:170–180. https://doi.org/10.1016/j.ijheatfluidflow.2013.05.021
Durst A, Wensing M, Berrocal E (2018) Light sheet fluorescence microscopic imaging for the primary breakup of diesel and gasoline sprays with real-world fuels. Appl Opt 57:2704–2714. https://doi.org/10.1364/AO.57.002704
Estrada-Pérez C, Hassan Y, Tan S (2011) Experimental characterization of temperature sensitive dyes for laser induced fluorescence thermometry. Rev Sci Instrum 82:074901. https://doi.org/10.1063/1.3590929
Fansler TD, Parrish SE (2014) Spray measurement technology: a review. Meas Sci Technol 26(1):012002. https://doi.org/10.1088/0957-0233/26/1/012002
Frackowiak B, Tropea C (2010) Numerical analysis of diameter influence on droplet fluorescence. Appl Opt 49(12):2363–2370. https://doi.org/10.1364/AO.49.002363
Gradeck M, Ouattara JA, Rémy B, Maillet D (2012) Solution of an inverse problem in the Hankel space—infrared thermography applied to estimation of a transient cooling flux. Exp Thermal Fluid Sci 36:56–64. https://doi.org/10.1016/j.expthermflusci.2011.08.003
Greenspan P, Fowler SD (1985) Spectrofluorometric studies of the lipid probe, Nile red. J Lipid Res 26:781–789
Huang C-Y, Murthy TG, Chandrasekar S (2014) Simultaneous measurements of thickness and temperature profile of the lubricant film at chip-tool interface during machining process using luminescent sensors. Proc Eng 79:9–16. https://doi.org/10.1016/j.proeng.2014.06.303
Jia W, Qiu HH (2003) Experimental investigation of droplet dynamics and heat transfer in spray cooling. Exp Thermal Fluid Sci 27(7):829–838. https://doi.org/10.1016/S0894-1777(03)00015-3
Kalathimekkad S, Missinne J, Schaubroeck D, Mandamparambil R, Van Steenberge G (2015) Alcohol vapor sensor based on fluorescent dye-doped optical waveguides. IEEE Sens J 15:76–81. https://doi.org/10.1109/JSEN.2014.2338916
Klinzing WP, Rozzi JC, Mudawar I (1992) Film and transition boiling correlations for quenching of hot surfaces with water sprays. J Heat Treat 9(2):91–103. https://doi.org/10.1007/BF02833145
Koegl M, Hofbeck B, Baderschneider K, Mishra YN, Huber FJT, Berrocal E, Will S, Zigan L (2018b) Analysis of LIF and Mie signals from single micrometric droplets for instantaneous droplet sizing in sprays. Opt Express 26(24):31750–31766. https://doi.org/10.1364/OE.26.031750
Koegl M, Mull C, Baderschneider K, Wislicenus J, Will S, Zigan L (2019a) Characterization of Nile red as a tracer for laser-induced fluorescence spectroscopy of gasoline and kerosene and their mixture with biofuels. Sensors 19(12):2822
Koegl M, Mishra YN, Storch M, Conrad C, Berrocal E, Will S, Zigan L (2019b) Analysis of ethanol and butanol direct-injection spark-ignition sprays using two-phase structured laser illumination planar imaging droplet sizing. Int J Spray Combus Dyn. https://doi.org/10.1177/1756827718772496
Koegl M, Mull C, Mishra YN, Will S, Zigan L (2020a) Characterization of fuel/water mixtures and emulsions with ethanol using laser-induced fluorescence. Appl Opt 59(4):1136–1144. https://doi.org/10.1364/AO.380392
Koegl M, Weiß C, Zigan L (2020b) Fluorescence Spectroscopy for Studying Evaporating Droplets Using the Dye Eosin-Y. Sensors. https://doi.org/10.3390/s20215985
Koegl M, Pahlevani M, Zigan L (2020c) A novel approach for measurement of composition and temperature of n-decane/butanol blends using two-color laser-induced fluorescence of Nile red. Sensors. https://doi.org/10.3390/s20195721
Koegl M, Dai H, Qomi MP, Bauer F, Eppinger B, Zigan L (2021) Morphology-dependent resonances in laser-induced fluorescence images of micrometric gasoline/ethanol droplets utilizing the dye nile red. Appl Opt 60(17):5000–5011. https://doi.org/10.1364/AO.423059
Koegl M, Delwig M, Zigan L (2022a) Characterization of fluorescence tracers for thermometry and film thickness measurements in liquid coolants relevant for thermal management of electric and electronic components. Sensors 22(22):8892
Koegl M, Dai H, Baderschneider K, Ulrich H, Zigan L (2022b) Polarization-dependent LIF/Mie ratio for sizing of micrometric ethanol droplets doped with Nile red. Appl Opt 61(14):4204–4214. https://doi.org/10.1364/AO.457685
Koegl M, Mishra YN, Hofbeck B, Baderschneider K, Huber FJT, Pracht J, Berrocal E, Will S, Zigan L (2018) 3D LIF/Mie planar droplet sizing in IC engine sprays using single-droplet calibration data In: ICLASS 2018: 14th International Conference on Liquid Atomization & Spray Systems, Chicago
Labergue A, Deprédurand V, Delconte A, Castanet G, Lemoine F (2010) New insight into two-color LIF thermometry applied to temperature measurements of droplets. Exp Fluids 49(2):547–556. https://doi.org/10.1007/s00348-010-0828-x
Labergue A, Gradeck M, Lemoine F (2015) Comparative study of the cooling of a hot temperature surface using sprays and liquid jets. Int J Heat Mass Transf 81:889–900. https://doi.org/10.1016/j.ijheatmasstransfer.2014.11.018
Lavieille P, Lemoine F, Lavergne G, Lebouché M (2001) Evaporating and combusting droplet temperature measurements using two-color laser-induced fluorescence. Exp Fluids 31:45–55. https://doi.org/10.1007/s003480000257
Lemoine F, Castanet G (2013) Temperature and chemical composition of droplets by optical measurement techniques: a state-of-the-art review. Exp Fluids. https://doi.org/10.1007/s00348-013-1572-9
Lin BS, Yang YC, Ho CY, Yang HY, Wang HY (2014) A PDMS-based cylindrical hybrid lens for enhanced fluorescence detection in microfluidic systems. Sensors 14(2):2967–2980. https://doi.org/10.3390/s140202967

Liu Y-C, Guessous L, Sangeorzan B, Alkidas A (2014) Laboratory experiments on oil-jet cooling of internal combustion engine pistons: area-average correlation of oil-jet impingement heat transfer. J Energy Eng. https://doi.org/10.1061/(ASCE)EY.1943-7897.0000227

Maligne D, Bruneaux G (2011) Time-resolved fuel film thickness measurement for direct injection si engines using refractive index matching. In: SAE 2011 World Congress and Exhibition, Detroit

Eastman chemical company, Marlotherm LH. Available online: https://www.eastman.com/Literature_Center/S/SFEHTF10985.pdf (19.07.2022)

McClintock PVE (2003) Cryogenics. In: Meyers RA (ed) Encyclopedia of physical science and technology, 3rd edn. Academic Press, New York, pp 37–59

Mishra YN, Abou Nada F, Polster S, Kristensson E, Berrocal E (2016) Thermometry in aqueous solutions and sprays using two-color LIF and structured illumination. Opt Express 24(5):4949–4963. https://doi.org/10.1364/OE.24.004949

Mishra YN, Koegl M, Baderschneider K, Hofbeck B, Berrocal E, Conrad C, Will S, Zigan L (2019) 3D mapping of droplet Sauter mean diameter in sprays. Appl Opt 58(14):3775–3783. https://doi.org/10.1364/AO.58.003775

Mishra YN, Yoganantham A, Koegl M, Zigan L (2020) Investigation of five organic dyes in ethanol and butanol for two-color laser-induced fluorescence ratio thermometry. Optics 1(1):1–17. https://doi.org/10.3390/opt1010001

Mouza A, Vlachos NA, Paras S, Karabelas A (2000) Measurement of liquid film thickness using a laser light absorption method. Exp Fluids 28:355–359. https://doi.org/10.1007/s003480050394

Nile red. Available online: https://www.carlroth.com/medias/SDB-7726-IE-EN.pdf?context=bWFzdGVyfHNlY3VyaXR5RGF0YXNoZWV0c3wyMjY2ODN8YXBwbGljYXRpb24vcGRmfHNlY3VyaXR5RGF0YXNoZWV0cy9oNWQvaDliLzg5NjUwMTE4MDAwOTQucGRmfGQzYzliZWViOGRlMDU5MGQ0MTMwMDk4YTkwODk5YTgxNGUyZjI2NmJiOTExMzk0Y2FiNzRiZjg0ZWY3OGU1ZGY (19.07.2022)

Palmer J, Reddemann MA, Kirsch V, Kneer R (2016) Temperature measurements of micro-droplets using pulsed 2-color laser-induced fluorescence with MDR-enhanced energy transfer. Exp Fluids 57(12):177. https://doi.org/10.1007/s00348-016-2253-2

Palmer J, Reddemann M, Kirsch V, Kneer R (2018) Applying 2D–2cLIF-EET thermometry for micro-droplet internal temperature imaging. Exp Fluids. https://doi.org/10.1007/s00348-018-2506-3

Pambudi NA, Sarifudin A, Firdaus RA, Ulfa DK, Gandidi IM, Romadhon R (2022) The immersion cooling technology: current and future development in energy saving. Alex Eng J 61(12):9509–9527. https://doi.org/10.1016/j.aej.2022.02.059

Pan R, Jeffries J, Dreier T, Schulz C (2016) Measurements of liquid film thickness, concentration, and temperature of aqueous urea solution by NIR absorption spectroscopy. Appl Phys B. https://doi.org/10.1007/s00340-015-6290-y

Pandey H, Kumar Gupta N (2022) A descriptive review of the thermal transport mechanisms in mono and hybrid nanofluid-filled heat pipes and current developments. Therm Sci Eng Prog 31:101281. https://doi.org/10.1016/j.tsep.2022.101281

Park S, Cho H, Yoon I, Min K (2002) Measurement of droplet size distribution of gasoline direct injection spray by droplet generator and planar image technique. Meas Sci Technol 13(6):859–864. https://doi.org/10.1088/0957-0233/13/6/305

Perrin L, Castanet G, Lemoine F (2015) Characterization of the evaporation of interacting droplets using combined optical techniques. Exp Fluids. https://doi.org/10.1007/s00348-015-1900-3

Prenting M, Dzulfida M, Dreier T, Schulz C (2020) Characterization of tracers for two-color laser-induced fluorescence liquid-phase temperature imaging in sprays. Exp Fluids. https://doi.org/10.1007/s00348-020-2909-9

Roe C, Feng X, White G, Li R, Wang H, Rui X, Li C, Zhang F, Null V, Parkes M, Patel Y, Wang Y, Wang H, Ouyang M, Offer G, Wu B (2022) Immersion cooling for lithium-ion batteries—a review. J Power Sources 525:231094. https://doi.org/10.1016/j.jpowsour.2022.231094

Schagen A, Modigell M, Dietze G, Kneer R (2006) Simultaneous measurement of local film thickness and temperature distribution in wavy liquid films using a luminescence technique. Int J Heat Mass Transf 49(25):5049–5061. https://doi.org/10.1016/j.ijheatmasstransfer.2006.06.010

Sick V, Stojkovic BD (2001) Evolution and impingement of an automotive fuel spray investigated with simultaneous Mie/LIF techniques. Appl Phys B. https://doi.org/10.1007/s003400100598

Ulrich H, Lehnert B, Guenot D, Svendsen K, Lundh O, Wensing M, Berrocal E, Zigan L (2022) Effects of liquid properties on atomization and spray characteristics studied by planar two-photon fluorescence. Phys Fluids 34:083305. https://doi.org/10.1063/5.0098922

Ulrich H, Sigl S, Möhnle M, Berrocal E, Zigan L (2023) Droplet thermometry based on an optimized two dye two-color laser-induced fluorescence concept. Front Phys. https://doi.org/10.3389/fphy.2023.1235847

Vetrano MR, Simonini A, Steelant J, Rambaud P (2013) Thermal characterization of a flashing jet by planar laser-induced fluorescence. Exp Fluids 54(7):1573. https://doi.org/10.1007/s00348-013-1573-8

Wolff M, Delconte A, Schmidt F, Gucher P, Lemoine F (2007) High-pressure Diesel spray temperature measurements using two-colour laser-induced fluorescence. Meas Sci Technol 18(3):697–706. https://doi.org/10.1088/0957-0233/18/3/020

Wu W, Kong S, Xu X, Tao J, Li C, Wang J, Su M, Yang H (2021) Simultaneous measurement of liquid film thickness and temperature on metal surface. Spectrochim Acta Part A Mol Biomol Spectrosc 257:119804. https://doi.org/10.1016/j.saa.2021.119804

Yang J, Melton LA (2000) Fluorescence-based method designed for quantitative measurement of fuel film thickness during cold-start of engines. Appl Spectrosc 54(4):565–574

Yang H, Wei W, Su M, Chen J, Cai X (2018) Measurement of liquid water film thickness on opaque surface with diode laser absorption spectroscopy. Flow Meas Instrum 60:110–114. https://doi.org/10.1016/j.flowmeasinst.2018.02.005

Zhang Y, Leng J, Hu W (2018) Theoretical design of a two-photon fluorescent probe for nitric oxide with enhanced emission induced by photoninduced electron transfer. Sensors. https://doi.org/10.3390/s18051324

Zhou J, Yang W, Yin Y, Chen S, Yan B, Mu J, Qi X (2019) Nonlinear temperature calibration equation for Rhodamine B in different solutions for wide-temperature-range applications. Appl Opt 58(6):1514–1518. https://doi.org/10.1364/AO.58.001514